



# Metamaterials for analog all-optical computation

Michele Cotrufo<sup>a</sup> and Andrea Alù<sup>b,c,\*</sup>

<sup>a</sup>The Institute of Optics, University of Rochester, Rochester , NY, United States

<sup>b</sup>Photonics Initiative, Advanced Science Research Center, City University of New York, New York, NY, United States

<sup>c</sup>Physics Program, Graduate Center of the City University of New York, New York, NY, United States

\*Corresponding author. e-mail address: [aalu@gc.cuny.edu](mailto:aalu@gc.cuny.edu)

## Contents

1. Introduction	212
2. Spatio-temporal image processing via metasurfaces	215
2.1 Mathematical background	215
2.2 Spatial operations	219
2.3 Temporal operations	230
2.4 Spatio-temporal operations	232
2.5 Pulse shapers and 4f optical systems with metasurfaces used as masks	236
3. Tunable computational metasurfaces	237
4. Nonlinear computational metamaterials	238
5. Final remarks and outlook	241
Acknowledgements	243
References	243

## Abstract

Analog-based all-optical computation has recently gained renewed interest due to the growing demand for data processing and the associated need for low-power, high-speed and compact computational platforms. While optical computing platforms based on bulky optical setups—such as 4f systems and pulse shapers—have been studied for decades, their large footprints have prevented their miniaturization and integration. Recently, a new all-optical computing platform has been proposed based on metamaterials—artificially structured materials with morphological features smaller than the radiation wavelength. By accurately tailoring their transfer function, it is possible to design metamaterials that perform computational tasks similar to their macroscopic counterparts, but within subwavelength footprints. In this chapter, we discuss the general working principle of these devices, their advantages and challenges, and the relevant figures of merit to be optimized. We also highlight specific examples and applications, providing a review of recent literature and an outlook on the field.

## 1. Introduction

Two well-known optical setups able to perform all-optical computation in the spatial and/or temporal domain consist of 4f optical systems and of pulse shapers (Fig. 1, top-middle). A 4f optical system (Fig. 1, top) is composed of an arrangement of two lenses placed two focal lengths away from each others (Goodman, 1996). An optical image  $f_{in}(x, y)$  is projected onto the front focal plane of the first lens. As well-known from Fourier optics (Goodman, 1996), the Fourier

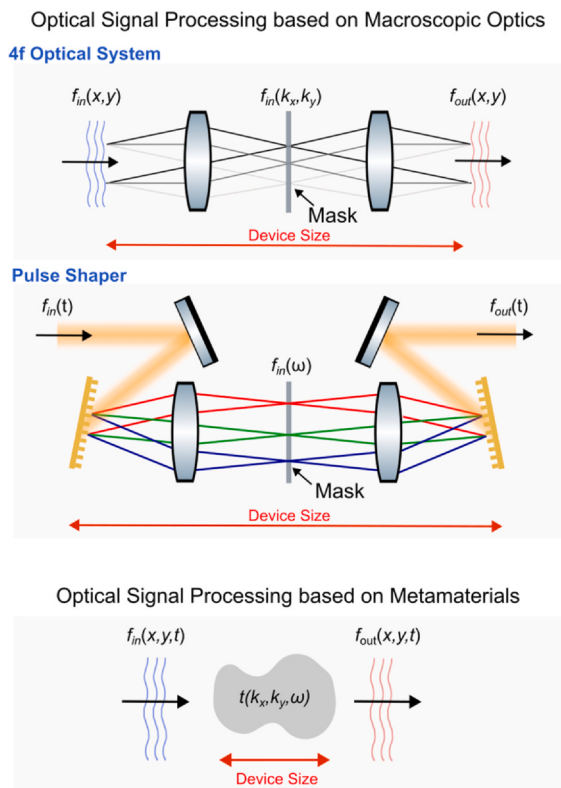


**Fig. 1** Top-Middle: Spatial and temporal signal processing can be performed with macroscopic optical systems such as, respectively, 4f systems (top) and pulse shapers (middle). In both cases, the input signal is decomposed into its Fourier components with the aid of macroscopic optics, and Fourier filtering is then performed with the aid of a spatially varying mask. Bottom: By tailoring the scattering response of a metamaterial, optical signal processing can be performed in much smaller footprints. The metamaterial acts directly on the Fourier components of the input signal.

transform  $f_{in}(k_x, k_y)$  of the input image is obtained at the back focal plane of the first lens, which coincides with the front focal plane of the second lens. At this plane, the complex electromagnetic field amplitude at each spatial point corresponds to the amplitude of a well-defined Fourier component of the image at the front focal plane of the first lens. Thus, by placing a spatially varying mask in this plane (e.g., a metallic mask with transparent apertures at desired locations), we can selectively transmit only certain Fourier components of the image, or selectively modify their weight, thus performing any desired linear image processing. The second lens then performs an anti-Fourier transform, creating the real-space processed image in its back focal plane. If the two lenses have the same focal length  $f$ , the total length of the system (from the plane of the input image to the plane of the output image) is  $4f$ . Common image processing tasks are blurring of the input image, which is achieved by blocking the Fourier components corresponding to high spatial frequencies, which may be obtained with an iris in the middle focal plane, or the enhancement of the edges of the input image, which is instead achieved by blocking the Fourier components corresponding to low spatial frequencies through a reflective disk instead of the iris.

A similar approach can be developed to process signals in the time domain, as commonly done with *pulse shapers* (Weiner, 2000, 2011; Weiner, Heritage, & Kirschner, 1988) (Fig. 1, middle). In this case, a time-dependent optical signal  $f_{in}(t)$  is sent on a diffraction grating which, together with a lens, can be used to make sure that, in a certain physical plane, each point corresponds to a different spectral component of the temporal Fourier transform  $f_{in}(\omega)$ . Similarly to the 4f system, a spatially varying mask can then be used to selectively filter or modify the different frequency components. Also here, the signal can be then collected by a second lens, and a second diffraction grating provides its anti-Fourier transform, creating a time-domain output signal  $f_{out}(t)$ . The use of pulse shapers to manipulate ultrafast optical signals has been pioneered by A. Weiner and collaborators (Weiner, 2000, 2011; Weiner et al., 1988). The overall footprint of the pulse shaper is again determined by the focal length of the involved lenses and by the resolving power level of the diffraction gratings.

While extremely versatile and easy to implement, both setups suffer from the fact that the overall footprint is inherently constrained by the need for bulky optical elements, such as lenses and diffraction gratings.

Fundamentally, large footprints are required because these devices do not operate directly into Fourier space. Instead, two additional steps are required, in order to first Fourier-transform the input signal and then anti-Fourier transform the filtered spectrum. As clear from the sketches in Fig. 1, these steps are typically the main elements contributing to the overall device footprint. In addition, alignment issues can become crucial in systems involving multiple devices operating in the far-field of each other, making the robustness of the whole setup often challenging. Such solutions are hardly compatible with the current needs for integration and compactness. These challenges have naturally led to the question as to whether it is possible to realize devices *that act directly in the Fourier domain of an incoming image*, that is, devices that are able to perform Fourier operations on an input signal *without having to first physically decompose the signal in the Fourier space and then map its Fourier decomposition on another plane*. About a decade ago it was suggested (Silva et al., 2014) that metamaterials—artificial materials composed of morphological features with typical sizes smaller than the radiation wavelength—may be used to perform Fourier-based filtering in much more compact footprints. Indeed, as schematically sketched in Fig. 1 (bottom), a metamaterial can be designed so that its transfer function—that is, how it transmits or reflects impinging radiation—is strongly dependent on the angle of excitation and/or the frequency, in a way that would not be possible with bulky naturally-available materials. Since angle- and frequency-dependent transfer functions directly map into the spatial and temporal Fourier components of the incoming signal, metamaterials can be engineered to impart nontrivial mathematical operations on input signals without needing to physically decompose the input signal into its spatial or spectral Fourier components—that is, without the need of additional macroscopic optical elements and within an extremely compact footprint.

In this chapter, we first provide a general tutorial and overview of the working principles of such image processing metamaterials, and we then explain how their transfer function may be tailored in order to implement general spatio-temporal mathematical operations. Next, we focus on specific scenarios recently studied in literature, and we provide a brief (non-exhaustive) review of recent works. While most of the results discussed in this chapter broadly apply to many types of metamaterials, here we mostly focus on so-called *metasurfaces*—that is, planarized patterned films that feature subwavelength thicknesses.



## 2. Spatio-temporal image processing via metasurfaces

We begin by explaining how a metasurface with tailored transfer function can be leveraged to implement arbitrary linear spatio-temporal transformations on the impinging field, without the need for additional bulky optical devices. We first provide a general mathematical background, and then we discuss specific examples and review relevant literature.

### 2.1 Mathematical background

In this section, we aim at determining the link between the vectorial transfer function  $\bar{t}(k_x, k_y, \omega)$  of a metasurface and the linear mathematical transformation performed by it on an input signal carried by a structured electromagnetic wave. Let us assume (Fig. 2) that a time-dependent optical image is defined in the plane  $z=0$  by an electric field  $\mathbf{E}_{\text{in}}(x, y, t) = E_{\text{in}}(x, y, t)\mathbf{e}_{\text{in}} = \mathcal{E}_{\text{in}}(x, y, t)e^{i\omega_0 t}\mathbf{e}_{\text{in}}$ , with polarization  $\mathbf{e}_{\text{in}} = [E_{0x}, E_{0y}]$ , carried by a wave with angular frequency  $\omega_0 = 2\pi c/\lambda = k_0 c$  and spatio-temporal envelope  $\mathcal{E}_{\text{in}}(x, y, t)$ . Following standard Fourier analysis, the image can be decomposed into a bundle of plane waves, each propagating along a direction identified by the polar and azimuthal angles  $\theta$  and  $\phi$  (Fig. 2). In particular, in the far field of the image ( $r \gg \lambda$ ) the field generated at a point identified by the

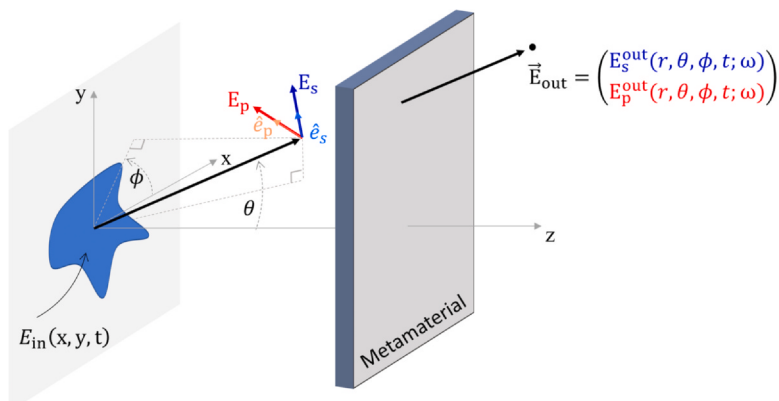


**Fig. 2** A spatio-temporal input signal can be decomposed into a bundle of plane waves, each propagating at a different angle and with a different frequency. The figure shows a specific plane wave with direction  $(\theta, \phi)$  and polarization  $E_p\hat{e}_p + E_s\hat{e}_s$ . After passing through a thin metamaterial, the wave amplitude and polarizations are changed.

spherical coordinates  $(r, \theta, \phi)$  and oscillating at frequency  $\omega = kc$  is given by (Collin, 1985)

$$\begin{aligned} \mathbf{E}(r, \theta, \phi, t; \omega) = \begin{pmatrix} E_s^{\text{in}}(t; \theta, \phi, \omega) \\ E_p^{\text{in}}(t; \theta, \phi, \omega) \end{pmatrix} &= ik \frac{e^{-i(kr-\omega t)}}{2\pi r} f_{\text{in}}(k_x, k_y, \omega) \\ &\quad \begin{pmatrix} \cos \phi & \sin \phi \\ -\cos \theta \sin \phi & \cos \theta \cos \phi \end{pmatrix} \begin{pmatrix} E_{0x} \\ E_{0y} \end{pmatrix} \end{aligned} \quad (1)$$



where  $f_{\text{in}}(k_x, k_y, \omega) \equiv \int dx dy dt e^{-i(k_x x + k_y y - \omega t)} E_{\text{in}}(x, y, t) = \int dx dy dt e^{-i(k_x x + k_y y - (\omega - \omega_0)t)} E_{\text{in}}(x, y, t)$  is the spatio-temporal Fourier transform of the input image, and  $E_{s/p}^{\text{in}}$  denote the s- and p-polarized components of the electric field. The wave vector components  $[k_x, k_y]$  depend on the angles  $(\theta, \phi)$  through the standard coordinate transformation  $k_x = k \sin \theta \cos \phi$ ,  $k_y = k \sin \theta \sin \phi$ . In the following formulas, we use the coordinates  $[k_x, k_y]$  and  $(\theta, \phi)$  interchangeably, with the implicit understanding that, for each plane wave, the modulus of the wave vector  $k$  depends on the frequency  $\omega$  via  $\omega = kc$ . We can rewrite Eq. 1 as

$$\begin{pmatrix} E_s^{\text{in}}(r, \theta, \phi, t; \omega) \\ E_p^{\text{in}}(r, \theta, \phi, t; \omega) \end{pmatrix} = ik \frac{e^{-i(kr-\omega t)}}{2\pi r} f_{\text{in}}(k_x, k_y, \omega) \begin{pmatrix} E_s(\theta, \phi) \\ E_p(\theta, \phi) \end{pmatrix} \quad (2)$$

where we defined  $E_p(\theta, \phi) = E_{0x} \cos \phi + E_{0y} \sin \phi$  and  $E_s(\theta, \phi) = E_{0y} \cos \phi - E_{0x} \sin \phi$ . The polarization of each wave in Eq. 2 is generally a mixture of s and p polarizations, depending on the polarization of the illumination and the direction of propagation. The response of the metasurface can be described by a  $2 \times 2$  matrix of transfer functions, each of them describing the frequency- angle-dependent transmission amplitudes for a given pair of impinging and outgoing polarizations,

$$\bar{t}(k_x, k_y, \omega) = \begin{pmatrix} t_{ss}(k_x, k_y, \omega) & t_{sp}(k_x, k_y, \omega) \\ t_{ps}(k_x, k_y, \omega) & t_{pp}(k_x, k_y, \omega) \end{pmatrix} \quad (3)$$

For example,  $t_{ss}(k_x, k_y, \omega)$  is equal to the amplitude of a transmitted s-polarized wave, due to an s-polarized wave with unity amplitude impinging on the metasurface at frequency  $\omega$  along the direction identified by  $(k_x, k_y)$ . The co-polarized functions  $t_{ss}$  and  $t_{pp}$  describe scattering

processes where the polarization is preserved, while the cross-polarized functions  $t_{sp}$  and  $t_{ps}$  describe polarization conversion. Generally, the field transmitted through the metasurface can be written as

$$\begin{aligned} \mathbf{E}_{\text{out}}(r, \theta, \phi, t; \omega) = \begin{pmatrix} E_s^{\text{out}}(r, \theta, \phi, t; \omega) \\ E_p^{\text{out}}(r, \theta, \phi, t; \omega) \end{pmatrix} &= ik \frac{e^{-i(kr - \omega t)}}{2\pi r} f_{in}(k_x, k_y, \omega) \\ &\quad \begin{pmatrix} t_{ss} & t_{sp} \\ t_{ps} & t_{pp} \end{pmatrix} \begin{pmatrix} E_s(\theta, \phi) \\ E_p(\theta, \phi) \end{pmatrix} \end{aligned} \quad (4)$$

Thus, an observer (either the human eye or an optical system) placed on the back of the metasurface sees a bundle of filtered plane waves, resulting in a processed spatio-temporal signal. To calculate the signal received by the observer, we exploit time-reversal symmetry and project all waves in Eq. 4 back to the plane  $z = 0$ . This procedure effectively removes the factor  $ik \frac{e^{-i(kr - \omega t)}}{2\pi r}$  in Eq. 4. Moreover, we transform the fields from the  $s$ - $p$  basis into the Cartesian  $x$ - $y$  basis. The required spatial transformation is the opposite of the one performed in Eq. 1,

$$\begin{pmatrix} E_x^{\text{out}}(\theta, \phi, \omega) \\ E_y^{\text{out}}(\theta, \phi, \omega) \end{pmatrix} = \bar{M}^{-1}(\theta, \phi) \left[ f_{in}(k_x, k_y, \omega) \begin{pmatrix} t_{ss} & t_{sp} \\ t_{ps} & t_{pp} \end{pmatrix} \begin{pmatrix} E_s(\theta, \phi) \\ E_p(\theta, \phi) \end{pmatrix} \right] \quad (5)$$

where  $\bar{M}^{-1}$  is the inverse of the matrix used in Eq. 1, that is,

$$\bar{M}(\theta, \phi) = \begin{pmatrix} \cos \phi & \sin \phi \\ -\cos \theta \sin \phi & \cos \theta \cos \phi \end{pmatrix} \quad (6)$$

Finally, the space- and time-dependent electric fields,  $E_x^{\text{out}}(x, y, t)$  and  $E_y^{\text{out}}(x, y, t)$ , which correspond to the electric field of the processed image, are obtained via the inverse Fourier transform,

$$E_{x/y}^{\text{out}}(x, y, t) = \frac{1}{2\pi} \int dx dy e^{i(k_x x + k_y y - \omega t)} E_{x/y}^{\text{out}}(k_x, k_y, \omega) \quad (7)$$

Thus, the output image in Eq. (7)—that is, the image seen by an observer placed on the right side of the metasurface—is given by a non-trivial combination of (i) the Fourier decomposition of the input image  $f_{in}(k_x, k_y, \omega)$ , (ii) the polarization of the input image  $\mathbf{e}_{\text{in}} = [E_{0x}, E_{0y}]$ , and (iii) the spatio-temporal and polarization-dependent transfer matrix of the metasurface (Eq. 3). At first sight, it is not clear how the scattering process

described by Eqs. 1–7 can be used to realize a useful signal processing. To get a better understanding, in the next subsections we consider specific scenarios of interest.

### 2.1.1 Polarization-independent response and absence of cross-polarized terms

Let us assume that the transfer matrix (Eq. 3) is polarization independent (i.e.,  $t \equiv t_{ss} = t_{pp}$ ) and that no polarization conversion occurs (i.e.,  $t_{sp} = t_{ps} = 0$ ). The matrix  $\bar{t}(k_x, k_y, \omega)$  can then be effectively replaced by a scalar function, and Eq. (5) can be rewritten as

$$\begin{pmatrix} E_x^{out}(\theta, \phi, \omega) \\ E_y^{out}(\theta, \phi, \omega) \end{pmatrix} = t(k_x, k_y, \omega) f_{in}(k_x, k_y, \omega) \begin{pmatrix} E_{0x} \\ E_{0y} \end{pmatrix} \quad (8)$$

where we have exploited the fact that the vector  $(E_s(\theta, \phi), E_p(\theta, \phi))^T$  is related to the vector  $(E_{0x}, E_{0y})^T$  via the matrix  $\bar{M}(\theta, \phi)$  in Eq. 1, which in turns cancels the term  $\bar{M}^{-1}(\theta, \phi)$  in Eq. (5). Thus, via Eq. (7), the space- and time-dependent electric fields are

$$\begin{pmatrix} E_x^{out}(x, y, t) \\ E_y^{out}(x, y, t) \end{pmatrix} = \frac{1}{2\pi} \begin{pmatrix} E_{0x} \\ E_{0y} \end{pmatrix} \int dx dy dt e^{i(k_x x + k_y y - \omega t)} t(k_x, k_y, \omega) f_{in}(k_x, k_y, \omega) \\ = \begin{pmatrix} E_{0x} \\ E_{0y} \end{pmatrix} \mathcal{F}^{-1}[t(k_x, k_y, \omega) f_{in}(k_x, k_y, \omega)] \equiv \begin{pmatrix} E_{0x} \\ E_{0y} \end{pmatrix} \mathcal{L}[E_{in}(x, y, t)] \quad (9)$$

where  $\mathcal{F}^{-1}$  denotes the inverse spatio-temporal Fourier transform, and in the last term we introduced the operator  $\mathcal{L}$  to describe the general transformation performed on the input field. Thus, each component of the output field is given by the inverse Fourier transform of the product between the Fourier transform of the input image  $f_{in}(k_x, k_y, \omega)$  and the scalar transfer function of the metasurface  $t(k_x, k_y, \omega)$ . Therefore, by exploiting the well-known correspondence between operators in real space (i.e., space and/or time dimensions) and in Fourier space (i.e., wavevector and frequency dimensions), any linear spatio-temporal operation (which we have denoted with  $\mathcal{L}$  in Eq. 9) can in principle be performed by tailoring the transfer function  $t(k_x, k_y, \omega)$ . Depending on the choice of the scalar transfer function  $t(k_x, k_y, \omega)$  in Eq. 9, different manipulations of the input signals can be obtained.

## 2.2 Spatial operations

We first consider the case of a frequency-independent transfer function,  $t(k_x, k_y, \omega) = t(k_x, k_y)$ . In this case, only the spatial components of the input field are manipulated by the metasurface. One of the simplest and most relevant examples of spatial operation of an image is differentiation. Differentiation operations in real space correspond to polynomial multiplicative factors in Fourier space, according to the correspondence  $\partial_q^m \rightarrow (ik_q)^m$ , where  $m \in \mathbb{N}$  and  $q = \{x, y\}$ . For example, a transfer function of the form  $t(k_x, k_y) = (ik_x)^m + (ik_y)^n$  results into an output image  $E^{out}(x, y) = (\partial_x^m + \partial_y^n)E^{in}(x, y)$ . Following the same approach, any combination of differential operators, including, for example, products of differential operators [ $E^{out}(x, y) = \partial_x^m \partial_y^n E^{in}(x, y)$ ] can be obtained by designing the transfer function accordingly. Among the many differential operations, the so-called Laplacian operation,  $\nabla^2 = \partial_x^2 + \partial_y^2$  has received particular attention in the literature. This is due to several reasons:

1. Calculating the Laplacian of an input image, that is  $f_{in}(x, y) \rightarrow f_{out}(x, y) = \nabla^2 f(x, y)$ , enhances the edges of the image. That is, the output image contains only the areas of the input image where the image amplitude is strongly varying in space. This operation, normally called *edge enhancement* or *edge detection*, can find practical applications in fields such as object recognition, currently of great relevance for autonomous vehicles that require fast processing of complex scenes in real-time.
2. The operation  $f_{in}(x, y) \rightarrow f_{out}(x, y) = \nabla^2 f(x, y)$  is isotropic with respect to rotations in the  $xy$  plane. That is, if the input image is rotated, the output image is also rotated, but otherwise remains the same. As a practical consequence, when applying the Laplacian operation, the edges of the input image  $f_{in}(x, y)$  are detected with the same efficiency, independently of their orientation. Other differential operators, such as  $\partial_x + \partial_y$ , are not isotropic: edges that are parallel to either the  $x$  or  $y$  axis are detected with different efficiencies than, for example, edges that are oriented along the  $xy$  diagonal.
3. The operator  $\nabla^2 = \partial_x^2 + \partial_y^2$  is also easy to implement, because the corresponding transfer function in Fourier space  $t(k_x, k_y) = -(k_x^2 + k_y^2)$  is a real-valued function. That is, it is not necessary to impart different phases onto different Fourier components of the input image, which often makes the design of the metasurface more cumbersome. Moreover, if we map the  $(k_x, k_y)$  coordinates onto the angles of the

corresponding impinging wave, we find that the transfer function can be written as  $t(\theta, \phi) \propto -\sin^2 \theta$ : the transmission amplitude should be zero at normal incidence  $\theta = 0$ , and it should increase quadratically with  $\theta$ , independently of  $\phi$ . As we discuss below, this behavior is relatively easy to obtain by working near the transmission zeros of resonant metasurfaces.

Indeed, several theoretical (Bykov, Doskolovich, Bezuš, & Soifer, 2014; Guo, Xiao, Minkov, Shi, & Fan, 2018; Kwon, Sounas, Cordaro, Polman, & Alù, 2018; Kwon, Cordaro, Sounas, Polman, & Alù, 2020; Silva et al., 2014; Xue & Miller, 2021; Zhu et al., 2019) and experimental (Cordaro et al., 2019; Cotrufo, Arora, Singh, & Alù, 2023; Cotrufo, Singh, Arora, Majewski, & Alù, 2023; Ji et al., 2022; Komar et al., 2021; Wesemann et al., 2019; Wesemann et al., 2021; Zhou, Zheng, Kravchenko, & Valentine, 2020; Zhu et al., 2017; Zhu et al., 2021) studies have demonstrated that the Laplacian operations (and other kinds of spatial operations) can be implemented with different types of nanophotonic materials and devices. In particular, several works have shown that periodic metasurfaces (Cordaro et al., 2019; Cotrufo, Arora et al., 2023; Cotrufo, Singh et al., 2023; Guo et al., 2018; Ji et al., 2022; Komar et al., 2021; Kwon et al., 2018, 2020; Zhou et al., 2020) can provide a highly-tailorable angular response, which is ideal to achieve the desired Fourier filtering. A common recipe to implement a spatial differential operator is to engineer the resonance spectrum of the metasurface to support a broad resonance feature (bright mode), coupled to a much sharper resonance (dark mode). Their interaction can produce a sharp *Fano resonance* profile in the transmission spectrum at normal incidence, which results in a sharp transmission dip and a peculiarly asymmetric response for neighboring frequencies (see, e.g., Fig. 3A, bottom-left plot). The fastly varying spectral features of the Fano lineshape are typically associated with a strong spatial dispersion, which implies that the resonant dip shifts as the polar angle of the excitation is varied. As a result, at a fixed frequency the transmission evolves from a low value (near zero) at normal incidence to a large value for large angles (see, e.g., Fig. 3A, bottom-right plot). Based on this principle, Cordaro et al. (2019) demonstrated a metasurface made of a 1D silicon grating (Fig. 3A) that can perform edge detection in the visible range, albeit with limited isotropy. Similar devices can also be used to perform phase imaging (Ji et al., 2022; Wesemann et al., 2021), that is, to enhance the phase discontinuities of images with otherwise constant amplitude. Zhou et al.

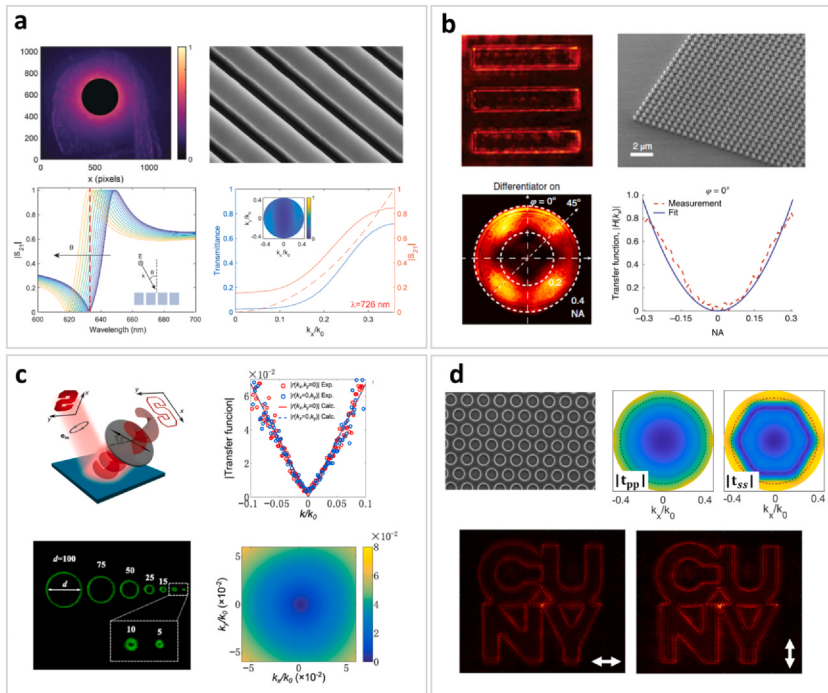


**Fig. 3** Spatial differentiation metasurfaces. (A) 1D silicon grating. (B) Square array of silicon pillars. (C) Air-Glass Interface. (D) Triangular lattice of holes etched into a silicon membrane. (A) Adapted with permission from Cordaro, A., Kwon, H., Sounas, D., Koenderink, A. F., Alù, A., & Polman, A. (2019). High-index dielectric metasurfaces performing mathematical operations. *Nano Letters*, 19(12), 8418–8423. (B) Adapted with permission from Zhou, Y., Zheng, H., Kravchenko, I. I., & Valentine, J. (2020). Flat optics for image differentiation. *Nature Photonics*, 14(5), 316–323. (C) Adapted with permission from Zhu, T., Guo, C., Huang, J., Wang, H., Orenstein, M., Ruan, Z., & Fan, S. (2021). Topological optical differentiator. *Nature Communications*, 12(1), 680. (D) Adapted with permission from Cotrufo, M., Arora, A., Singh, S., & Alù, A. (2023). Dispersion engineered metasurfaces for broadband, high-NA, high-efficiency, dual-polarization analog image processing. *Nature Communications*, 14(1), 7078.

proposed a different metasurface design (Zhou et al., 2020) based on a square array of pillars (Fig. 3B), which performs edge detection for unpolarized light over a large operational bandwidth, thanks to a low-Q-factor optical resonance, and with improved isotropy thanks to the C4 rotational symmetry of their design. A similar design, based on a square array of particles supporting Mie-type resonances, has also been proposed by Komar and co-authors (Komar et al., 2021). In another recent work

(Cotrufo, Arora et al., 2023), a silicon metasurface made of a triangular array of holes (Fig. 3D) was shown to perform polarization-independent edge detection over large numerical apertures, with almost perfect isotropy, and over moderately large spectral bandwidths. The desired angle-dependent response can also be obtained with devices different than thin patterned films. For example, approaches based on topological photonics (Zhu et al., 2017, 2021) (Fig. 3D) can provide broad spectral bandwidths and better isotropy, although they typically suffer from low efficiencies, as they require working in a cross-polarized reflection modality. On-demand angle-dependent transmission profiles can also be obtained by engineering multilayer films (Xue & Miller, 2021), although at the expense of increased transversal thicknesses.

Focusing on the Laplacian operation, next we discuss the relevant metrics of performance and underlying trade-offs in the design of image processing metasurfaces. Similar concepts and challenges discussed in the following can be applied to other operations.

### **2.2.1 Relevant figures of merit**

As discussed above, several physical mechanisms can be exploited to design metasurfaces whose transfer function is close to the one required to implement the Laplacian operation. The fundamental ingredient to obtain edge detection—that is, that the transmission is zero at normal incidence and it progressively increases with the incidence angle—is relatively easy to achieve with resonant metasurfaces. Nonetheless, there are several figures of merit that needs to be carefully assessed and optimized if these devices have to become relevant for practical applications. As summarized in Fig. 4, we identify at least five relevant figures of merit that need to be considered in the design of image processing metasurfaces:

- 1. Spectral bandwidth.** The desired angle-dependent transmission profile can be obtained by engineering the spatial dispersion of metasurfaces through sharp resonances. However, this approach comes at the cost of a reduced spectral bandwidth. Indeed, a tailored dispersion in angle typically translates in a correlated dispersion in frequency, which limits the bandwidth of operation of these metasurfaces. Thus, often the desired operation on the incoming image can only be successfully performed within a narrow range of input frequencies. By considering multiple resonances and tailoring the frequency dispersion of the involved modes can broaden the bandwidth of operation (Cotrufo, Arora et al., 2023).

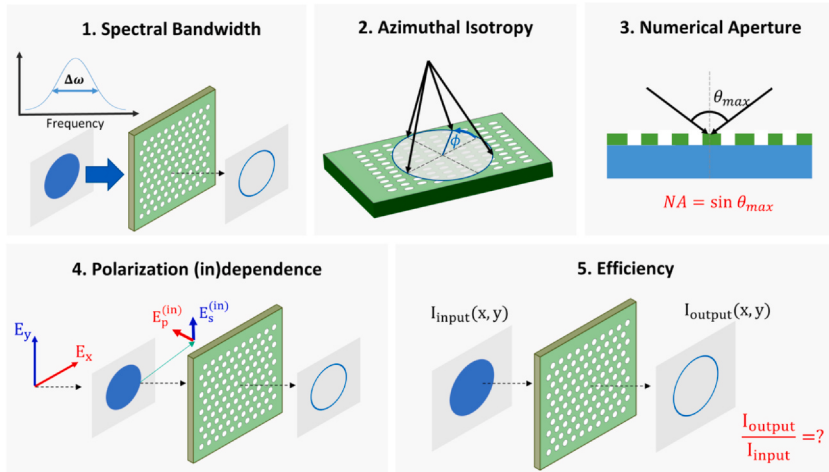


**Fig. 4** Key performance metrics for the use of computational metasurfaces in real-world applications.

**2. Isotropic response.** The transfer function required to implement the Laplacian operator,  $t(\theta, \phi) \propto -\sin^2 \theta$ , is independent of the azimuthal angle  $\phi$ . Thus, the response of the metasurface should ideally match this isotropy, that is, the metasurface transmission amplitude should remain unchanged for rotations of the impinging wave vector around the optical axis. Periodic metasurfaces typically break this symmetry, and choosing a highly symmetric lattice geometry is essential to maximize the isotropy. For instance, the first demonstrations of image processing metasurfaces involved lower-symmetry geometries, such as 1D gratings (Cordaro et al., 2019; Ji et al., 2022) and square lattices (Komar et al., 2021; Zhou et al., 2020), which negatively impact the isotropy of the response. The highest-order rotation symmetry group compatible with a periodic lattice is  $C_6$ , which corresponds to a triangular lattice. Thus, periodic metasurfaces with a  $C_6$  rotational symmetry are expected to provide the best isotropy under azimuthal rotations. In particular, the  $C_6$  symmetry guarantees that the metasurface response is perfectly isotropic at  $\theta \approx 0^\circ$ . Indeed, metasurfaces made of triangular lattices of holes (Cotrufó, Arora et al., 2023; Cotrufó, Singh et al., 2023; Kwon et al., 2020) have been shown to feature almost-perfect isotropy within a discretely large cone of angles  $0 < \theta < 20^\circ$ . Eventually, as the angle  $\theta$  increases further, it becomes challenging to maintain high isotropy, because tilted excitation directions are more sensitive to the lattice granularity.

- 3. Numerical aperture.** The plane waves associated with the input image are characterized by different in-plane wavevector moduli  $k_{\parallel} = \sqrt{k_x^2 + k_y^2} \leq k_0$ , and waves with larger  $k_{\parallel}$  carry information about smaller spatial features of the input image. In order to ensure that an arbitrary optical image is correctly processed, the metasurface transfer function should be able to reproduce the desired Fourier-space filtering (e.g.,  $t(k_x, k_y) = -(k_x^2 + k_y^2) = -k_{\parallel}^2$ ) for arbitrarily large values of  $k_{\parallel} \leq k_0$ . For the case of the Laplacian operator, this means that the ideal transmission amplitude  $t(\theta, \phi) \propto -\sin^2 \theta$  should be maintained for any  $\theta \leq 90^\circ$ . This is typically very challenging using periodic metasurfaces that rely on spatially dispersive modes, because at large angles the transmission  $|t(\theta, \phi)|^2$  is affected by other modes. Similar to standard objective lenses we can define a numerical aperture (NA) for image processing metasurfaces,  $NA = \sin \theta_{\max}$ , where  $\theta_{\max}$  is the largest polar angle at which the desired transfer function is achieved. For a given NA, the metasurface correctly processes input images only if the Fourier decomposition of the input image does not contain spatial frequencies with  $k_{\parallel} > NA \cdot k_0$ . Experimentally, NAs of 0.3–0.4 (corresponding to  $\theta_{\max} = 20^\circ$ – $30^\circ$ ) have been demonstrated in edge-detection metasurfaces ([Cordaro et al., 2019](#); [Cotrufo, Arora et al., 2023](#); [Cotrufo, Singh et al., 2023](#); [Komar et al., 2021](#); [Zhou et al., 2020](#)).
- 4. Polarization dependence.** When deriving Eq. 9 we have assumed that the response of the metamaterial is polarization-independent, that is,  $t \equiv t_{ss} = t_{pp}$  and that no polarization conversion occurs, that is,  $t_{sp} = t_{ps} = 0$ . These features are typically hard to achieve in metasurfaces. Indeed, the electromagnetic response of metasurfaces is typically different for *s*- and *p*-polarizations, especially for large values of polar angles  $\theta$ . Polarization mixing, that is,  $t_{sp} \neq 0$ ,  $t_{ps} \neq 0$  is also expected for  $\theta > 0$ , even in the case of highly symmetric designs satisfying C<sub>6</sub> rotational symmetry. Methods to mitigate this issue, based on engineering the metasurface dispersion ([Cotrufo, Arora et al., 2023](#)), have been proposed and demonstrated, yet a general and optimal solution to this issue is still lacking. Interestingly, large polarization asymmetry, that is,  $t_{ss} \neq t_{pp}$ , can actually be leveraged for polarization imaging ([Cotrufo, Singh et al., 2023](#)), as discussed in the next section.
- 5. Efficiency.** The throughput efficiency of the image processing process—that is, how the intensity of the output image compares to the intensity of the input image—is of paramount importance for practical applications, yet it is often overlooked in both theoretical and

experimental works on image processing metasurfaces. As we have discussed, there are different ways to design a metasurface that features a transfer function proportional to the desired one—for example  $t(\theta, \phi) = A(k_x^2 + k_y^2)$  for the Laplacian—where  $A$  is a complex proportionality coefficient. The output image provided by this transfer function carries the Laplacian of the input image, multiplied by the proportionality constant  $|A|^2$ . Low values of  $|A|$  are obviously detrimental because they reduce the intensity of the output image, thus requiring, for example, longer integration times in acquisition systems, higher input powers, or electronic amplification. The throughput efficiency is typically determined by different factors, including insertion loss (such as internal absorption and unwanted reflection), and sub-ideal transmission profiles, especially at large angles.

Defining a universal metric to assess the throughput efficiency can be tricky, since most definitions are affected by the type of input function used as a test. For instance, for edge detection most of the input power is rejected by the metasurface because of its functionality, since only the edges are supposed to be transmitted. In Ref. [Cotrufo, Arora et al. \(2023\)](#), two relevant efficiency metrics were introduced in this context. The *peak efficiency* is defined as the ratio  $\eta_{\text{peak}} \equiv \max(I_{\text{out}})/\max(I_{\text{in}})$  between the peak intensities in the recorded output and input images, hence estimating how much of the power density at the edge location is effectively transmitted. This metric can be easily estimated in experiments, however it tends to over-estimate the global intensity throughput. For this reason, the authors in Ref. [Cotrufo, Arora et al. \(2023\)](#) also defined the *average efficiency*  $\eta_{\text{avg}} \equiv \text{avg}(I_{\text{out}}^{\text{edge}})/\max(I_{\text{in}})$ , where  $\text{avg}(I_{\text{out}}^{\text{edge}})$  is the average intensity of the output image calculated only in narrow regions surrounding the expected positions of all edges. In the associated experiments in Ref. [Cotrufo, Arora et al. \(2023\)](#), values of  $\eta_{\text{peak}} \geq 5\%$  and  $\eta_{\text{avg}} \geq 1\%$  were achieved. It was also shown that, for the input image considered in that work and for the particular value of metasurface NA, the maximum theoretical peak efficiency was  $\eta_{\text{peak}}^{\text{theor}} \approx 20\%$ , thus not far from the measured one. However, we emphasize that these metrics, while useful, depend on the type of spatial features contained in the input image and on the image size (e.g., input images with sharper intensity variations lead to larger gradients). Thus,  $\eta_{\text{peak}}$  and  $\eta_{\text{avg}}$  can be used to compare the performance of two different metasurfaces only if all other experimental settings (including the shape of the

input image) are the same, and are expected to change, albeit not dramatically, for different images.

The five metrics of performance outlined above are all relevant and, ideally, they should be simultaneously optimized in order to realize devices of practical use. Unfortunately, there are several trade-offs involved in the design process, that is, when optimizing one of them we may need to make another one worse. For example, the spectral bandwidth can be increased by working with optical modes with larger linewidths, in order to increase the range of frequencies at which the normal-incidence transmission is low. However, optical modes with larger bandwidths also lead to a slower increase of transmission as the angle  $\theta$  increases. In turn, this can reduce the transmission of the high-spatial-frequency components, indicating a trade-off between spectral bandwidth and intensity throughput. Similarly, the numerical aperture can be in principle increased by engineering the metasurface dispersion in order to control more accurately the spectral shift of the target optical mode, and to avoid the occurrence of other unwanted modes in the spectral range of interest. However, as the NA increases it becomes challenging to also maintain large azimuthal isotropy and polarization independence. Approaches to mitigate these issues based on dispersion engineering have been proposed (Cotrufo, Arora et al., 2023). Nonetheless, a general route to optimize all these metrics fully and independently is currently lacking.

### **2.2.2 Metasurfaces with large polarization asymmetry**

It is often desirable to work with metasurfaces offering a polarization-independent response (i.e.,  $t \equiv t_{ss} = t_{pp}$ ). This ensures that, independently of the polarization and orientation of the input image, the output image carries the desired operation. In the specific case of Laplacian metasurfaces for edge detection, such polarization-independence ensures that all edges are detected with the same efficiency, independent of their orientation. Interestingly, while large polarization asymmetries are detrimental for isotropic edge detection, they can be leveraged to realize edge-detection devices that selectively enhance only certain edges, as a function on their orientation, as proposed in Ref. Cotrufo, Singh et al. (2023). This functionality is particularly interesting in the context of crowded and complex scenes, for which polarization imaging tools can offer a way to selectively enhance specific edges of interest (He et al., 2021; Rubin et al., 2022; Solomon, 1981; Tyo, Rowe, Pugh, & Engheta, 1996). In order to model the response of a polarization-selective image-processing metasurface, we

follow the derivation in Ref. Cotrufo, Singh et al. (2023) and rewrite Eq. 2 as a function of the in-plane wave vector  $\mathbf{k}_{\parallel} = (k_x, k_y)$ :

$$\mathbf{E}_{in}(\mathbf{k}_{\parallel}) = \begin{pmatrix} E_s^{in}(\mathbf{k}_{\parallel}) \\ E_p^{in}(\mathbf{k}_{\parallel}) \end{pmatrix} = f_{in}(\mathbf{k}_{\parallel}) \begin{pmatrix} \frac{k_z}{k_0} (\hat{\mathbf{k}}_{\parallel} \times \hat{\mathbf{e}}_{in})_z \\ \hat{\mathbf{k}}_{\parallel} \cdot \hat{\mathbf{e}}_{in} \end{pmatrix} \quad (10)$$

where we have removed all the dependencies on time and frequency  $\omega$  (since we are considering only spatial operations and monochromatic signals), and we also removed an overall constant factor for brevity. We have defined the directional vectors  $\hat{\mathbf{k}}_{\parallel} \equiv \mathbf{k}_{\parallel}/|\mathbf{k}_{\parallel}|$  and  $\hat{\mathbf{e}}_{in} = \mathbf{e}_{in}/|\mathbf{e}_{in}|$ , the  $z$ -component of the wave vector  $k_z = \sqrt{k_0^2 - |\mathbf{k}_{\parallel}|^2}$ , and the notation  $(...)_z$  denotes the  $z$  component of the vector inside the brackets. The expression in the right-hand-side of Eq. 10 corresponds to the standard decomposition into the  $s$ - and  $p$ -polarization basis. The transmitted field (Eq. 4) now reads

$$\mathbf{E}_{out}(\mathbf{k}_{\parallel}) = \begin{pmatrix} E_s^{out}(\mathbf{k}_{\parallel}) \\ E_p^{out}(\mathbf{k}_{\parallel}) \end{pmatrix} = f_{in}(\mathbf{k}_{\parallel}) \begin{pmatrix} t_{ss}(\mathbf{k}_{\parallel}) & t_{sp}(\mathbf{k}_{\parallel}) \\ t_{ps}(\mathbf{k}_{\parallel}) & t_{pp}(\mathbf{k}_{\parallel}) \end{pmatrix} \begin{pmatrix} \frac{k_z}{k_0} (\hat{\mathbf{k}}_{\parallel} \times \hat{\mathbf{e}}_{in})_z \\ \hat{\mathbf{k}}_{\parallel} \cdot \hat{\mathbf{e}}_{in} \end{pmatrix} \quad (11)$$

Let us now assume that the polarization response of the metasurface is strongly asymmetric. For example, consider the case in which  $t_{pp}(\mathbf{k}_{\parallel}) = t_{ps}(\mathbf{k}_{\parallel}) = t_{sp}(\mathbf{k}_{\parallel}) = 0$  for any impinging angle, while  $t_{ss}(\mathbf{k}_{\parallel})$  features the desired Fourier-space high-pass filtering. In other words, the device completely suppresses any incoming  $p$ -polarized wave, while it correctly processes  $s$ -polarized waves, and no polarization conversion occurs. Eq. 11 becomes

$$\mathbf{E}_{out}(\mathbf{k}_{\parallel}) = f_{in}(\mathbf{k}_{\parallel}) t_{ss}(\mathbf{k}_{\parallel}) \begin{pmatrix} \frac{k_z}{k_0} (\hat{\mathbf{k}}_{\parallel} \times \hat{\mathbf{e}}_{in})_z \\ 0 \end{pmatrix} = f_{in}(\mathbf{k}_{\parallel}) t_{ss}(\mathbf{k}_{\parallel}) \frac{k_z}{k_0} (\hat{\mathbf{k}}_{\parallel} \times \hat{\mathbf{e}}_{in})_z \hat{\mathbf{e}}_s \quad (12)$$

where we have introduced the  $s$ -polarization vector  $\hat{\mathbf{e}}_s$ . Because of the term  $\hat{\mathbf{k}}_{\parallel} \times \hat{\mathbf{e}}_{in}$ , all the Fourier components  $f_{in}(\mathbf{k}_{\parallel})$  corresponding to vectors  $\mathbf{k}_{\parallel}$  parallel to the impinging polarization  $\hat{\mathbf{e}}_{in}$  are not transmitted, thus not contributing to the output image. This effect becomes important when the input image  $E_{in}(x, y)$  contains an edge oriented along a certain direction  $\hat{\mathbf{n}}$ . In the limit of an infinitely long edge parallel to  $\hat{\mathbf{n}}$ , the Fourier transform  $f_{in}(\mathbf{k}_{\parallel})$  is non-zero only when  $\mathbf{k}_{\parallel}$  is orthogonal to  $\hat{\mathbf{n}}$ . By combining this result with eq. 12, we find that

$$\mathbf{E}_{out}(\mathbf{k}_{||}) = f_{in}(\mathbf{k}_{||}) t_{ss}(\mathbf{k}_{||}) \frac{k_z}{k_0} (\hat{\mathbf{n}} \cdot \hat{\mathbf{e}}_{in}) \hat{\mathbf{e}}_s \quad (13)$$

that is, the edges parallel to the input polarization ( $\hat{\mathbf{n}} \cdot \hat{\mathbf{e}}_{in} = 1$ ) maximally contribute to the output image, while the edges with direction orthogonal to the input polarization ( $\hat{\mathbf{n}} \cdot \hat{\mathbf{e}}_{in} = 0$ ) do not contribute. The opposite scenario occurs if the metasurface works only for *p*-polarization, that is, if only  $t_{pp}(\mathbf{k}_{||}) \neq 0$ . In this case

$$\mathbf{E}_{out}(\mathbf{k}_{||}) = f_{in}(\mathbf{k}_{||}) t_{pp}(\mathbf{k}_{||}) [(\hat{\mathbf{n}} \times \hat{\mathbf{e}}_{in})_z] \hat{\mathbf{e}}_p \quad (14)$$

and edges with direction parallel to the input polarization ( $\hat{\mathbf{n}} \times \hat{\mathbf{e}}_{in} = 0$ ) do not contribute to the output image. Equations 13–14 show that, by introducing polarization selectivity, that is, by realizing a metasurface for which  $t_{pp}(\mathbf{k}_{||})$  or  $t_{ss}(\mathbf{k}_{||})$  is very low for all input transverse momenta, while the other one provides the required Fourier filtering, it is possible to selectively enhance only the edges of an input image oriented along a desired direction. Since this direction is determined by the input polarization, we can then tune it in real-time, enabling polarization imaging operations. Notice that a polarization selective metasurface can still be fully isotropic, which is important for imaging applications, enabling the detection of edges with specific orientation independently of their position and of the metasurface orientation. This principle of operation has been experimentally demonstrated in Ref. Cotrufo, Singh et al. (2023), see figure Fig. 5. A metasurface, made of a triangular array of holes etched in a silicon slab, was designed (Fig. 5A–D) such that, at a given wavelength, the *s*-polarized transmission featured the desired Laplacian-like behavior  $t_{ss}(\mathbf{k}_{||}) \propto |\mathbf{k}_{||}|^2$  (Fig. 5B–C), while the *p*-polarized transmission remained almost zero across the same angular range (Fig. 5B,D). The imaging experiments confirm that, when the input image (Fig. 5E) is linearly polarized, the edges in the output images (Fig. 5G–H) are selectively enhanced only when parallel to the input polarization, following Eq. 13. For unpolarized illumination, all edges were enhanced with the same efficiency (Fig. 5F).

### 2.2.3 Coherent versus incoherent illumination

It is important to emphasize that the mathematical operations described in Eq. 9 acts on the amplitude of the field, and not on its intensity. In other words, after ignoring the vectorial nature of the field, Eq. 9 can be rewritten as

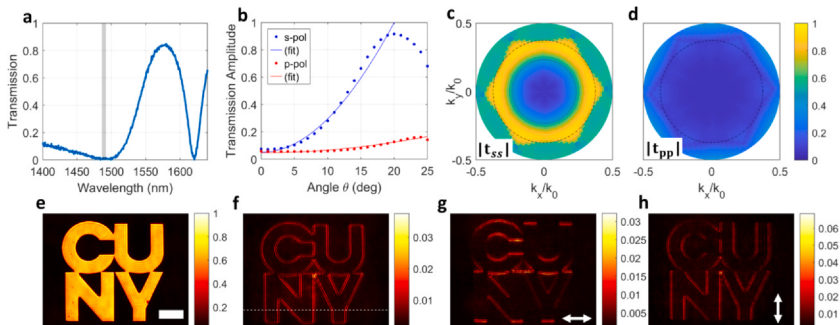


**Fig. 5** Impact of polarization asymmetries on the response of an edge-detecting metasurface. (A) Normal-incidence transmission spectrum of the metasurface. (B) s- and p-polarized transmission amplitudes versus  $\theta$  and for  $\phi = 0$ , for a wavelength corresponding to the grey area in panel a. (C–D) Full-angle s-polarized (panel c) and p-polarized (panel d) transmission amplitude. (E) Test image used in the experiment. (F) Output image obtained when the input image is made of unpolarized light. (G–H) Output images obtained when the input image is x-polarized (panel G) or y-polarized (panel H). Adapted with permission from Cotrufo, M., Singh, S., Arora, A., Majewski, A., & Alù, A. (2023). *Polarization imaging and edge detection with image-processing metasurfaces*. *Optica*, 10(10), 1331–1338.

$$E_{out}(x, y, t) = \mathcal{L}[E_{in}(x, y, t)] \quad (15)$$

which, in general, does not correspond to a linear operation between the field intensities  $I_{out} = |E_{out}(x, y, t)|^2$  and  $I_{in} = |E_{in}(x, y, t)|^2$ . Hence, the operation imparted by the metasurface on the image is strongly sensitive to the phase of the input field and, therefore, to its coherence. This has important advantages and disadvantages. On one hand, being able to operate directly on the field amplitude allows realizing operations that depend on the phase profile of the input. If the operation  $\mathcal{L}$  is a spatial derivative, for example,  $\mathcal{L} = \frac{d}{dx}$ , the resulting output intensity is

$$\begin{aligned} I_{out} &= |E_{out}(x, y)|^2 = |\mathcal{L}[E_{in}(x, y)]|^2 \\ &= |\mathcal{L}[|E_{in}(x, y)|e^{i\phi(x, y)}]|^2 \\ &= \left[ \frac{d}{dx}(|E_{in}(x, y)|) + i\frac{d}{dx}\phi(x, y) \right]^2 \end{aligned} \quad (16)$$

where we have written the field envelope as  $|E_{in}(x, y)|e^{i\phi(x, y)}$ . Thus, the output intensity contains information about the phase gradient, which may be exploited for applications such as phase imaging (Ji et al., 2022; Wesemann et al., 2021). This phase information would not be available if

$\mathcal{L}$  acted directly on the intensity of the input image. On the other hand, the fact that the linear operation imparted by the metamaterial acts on the field amplitude also dictates that the input illumination must be at least partially coherent. This is also clear from the fact that the derivation of Eq. 9 requires decomposing waves into their Fourier components and then recombining them coherently after filtering. This requires that the phase relationship between different Fourier components is well-defined, and it remains constant in space and time. Thus, this approach for analog computation is expected to fail if the input signal is incoherent. Recent works have proposed ways to overcome this limitation (Wang, Guo, Zhao, & Fan, 2020; Zhang, Bai, Sun, Jin, & Valentine, 2022), albeit at the expense of increased footprint and the requirement of digital postprocessing.

### 2.3 Temporal operations

We can return to the general result in Eq. 9, and now assume that the metasurface transfer functions are independent of  $k_x$  and  $k_y$ , that is,  $t(k_x, k_y, \omega) = t(\omega)$ , or equivalently that the input image is not spatially structured, that is,  $E_{in}(x, y, t) = E_{in}(t)$ , so that we can set  $f_{in}(k_x, k_y, \omega) = f_{in}(\omega)\delta(k_x)\delta(k_y)$ . In this case, the metamaterial performs a time-domain operation on the temporal input pulse  $E_{in}(t)$ ,

$$\begin{pmatrix} E_x^{out}(t) \\ E_y^{out}(t) \end{pmatrix} = \begin{pmatrix} E_{0x} \\ E_{0y} \end{pmatrix} \mathcal{F}^{-1}[t(\omega)f_{in}(\omega)] \quad (17)$$

Following the same approach as in the previous section, different linear operations in the time domain can be realized by calculating their corresponding multiplicative factor in Fourier space, and then encoding this factor into the transfer function of the metasurface  $t(\omega)$ . These operations replace the functionality of a bulky pulse shaper as in Fig. 1 with a tailored metasurface response.

Time-domain differential operators acting on the pulse envelope  $E_{in}(t)$  can be implemented according to the correspondence  $\left(\frac{d}{dt}\right)^m \rightarrow [(-i(\omega - \omega_0))^m]$ , where  $\omega_0$  is the wave carrier frequency. Differential operations of this type can be realized by engineering a metasurface that supports a transmission zero at  $\omega = \omega_0$ , and with a transmission amplitude increasing for frequencies smaller or larger than  $\omega_0$ . For example, the first-order time derivative requires  $t(\omega) = -i(\omega - \omega_0)$ , which can be readily obtained by engineering resonances with Lorentzian-like transmission

lineshapes. The  $\pi$  phase jump required as  $(\omega - \omega_0)$  changes sign can be readily obtained by leveraging the phase shift experienced by light transmitted through resonators as the frequency is swept across the resonant frequency. In this simplified scenario of temporal-only operations, some of the figures of merit discussed above are not particularly relevant, especially if one can assume that the input signal impinges on the metasurface always along the normal direction. For example, the numerical aperture  $NA = \sin \theta_{\max}$  and azimuthal isotropy are no longer relevant, since the input image is not spatially structured, and only the metasurface response at normal-incidence matters. Similarly, polarization asymmetries are typically less important, since it is relatively easy to design metasurfaces that are polarization independent at normal incidence. Even when the metasurface response is polarization-dependent at normal incidence, we can always rotate or project the polarization of the input signal to match the optimal one. The spectral bandwidth and throughput efficiency, instead, remain important in this scenario. In particular, the spectral bandwidth is fundamentally limited by the fact that we are performing Fourier filtering in the frequency domain, which requires a frequency-dependent transfer function. Indeed, the requirement that the transmission varies with frequency (e.g.,  $t(\omega) = -i(\omega - \omega_0)$ ) implies that the imparted operation is different if the input signal has a carrier frequency different than  $\omega_0$ . The intensity throughput, that is, the power carried by the output signal  $\int dt |E_{\text{out}}(t)|^2$  compared to the input signal  $\int dt |E_{\text{in}}(t)|^2$ , is affected both by the properties of the desired mathematical operation, and by nonidealities in the metasurface transfer function.

In addition, similar to what discussed for the case of spatial-only operations, often the metasurface transfer function is only *proportional* to the desired one, for example,  $t(\omega) = A(\omega - \omega_0)^m$ . While the output field is still proportional to the desired mathematical operation, low values of  $|A|$  introduce inefficiencies. In this context, in realistic settings the desired transfer function  $t(\omega)$  cannot be obtained over an arbitrarily large range of frequencies, due to practical limitations related to the achievable spectral linewidths and to fundamental limitations due to passivity and causality. In passive devices,  $|t(\omega)| \leq 1$ . Thus, transfer functions such as  $t(\omega) = A(\omega - \omega_0)^m$  can be realized over a bandwidth  $B \equiv 2 |\omega_{\max} - \omega_0|$  only if the coefficient  $|A|$  is low enough such that  $|A| \cdot |\omega_{\max} - \omega_0|^m \leq 1$ . This effectively introduces a trade-off between the bandwidth  $B$  of the input signal (i.e., the range of

frequency  $\omega$  over which the Fourier transform of the input signal  $|f_{in}(\omega)|$  is non-negligible) and the throughput efficiency.

Following this approach, recent theoretical (Knightley, Yakovlev, & Pacheco-Peña, 2022; Momeni, Rouhi, & Fleury, 2022; Tahmasebi, Abdolali, Rajabalipanah, Momeni, & Fleury, 2022) and experimental (Cotrufo, Esfahani, Korobkin, & Alù, 2024; Li et al., 2022a; Sol, Smith, & del Hougne, 2022) works have demonstrated the use of metasurfaces for analog signal processing in compact devices. Knightley and co-authors (Knightley et al., 2022) have numerically demonstrated a multilayered structure optimized such that, when an input signal impinges on it, the reflected signal is equal to the first-order time derivative of the input signal (Fig. 6A). Momeni et al. (2022) have considered a multi-layered patterned device, operating in the THz range, which can impart either temporal or spatial differentiations (Fig. 6B). In a recent experimental work, Sol and co-authors (Sol et al., 2022) have demonstrated a programmable metasurface that performs analog differentiation of input radio-frequency signals (Fig. 6C). Recently, Cotrufo et al. (2024) have demonstrated an optical metasurface performing analog differentiation on signals carried by near-visible frequencies (Fig. 6D). In this experiment it was also shown that, thanks to their ultrathin profile and to the transmissive operation, these devices can be cascaded to realize more complex operations. For example, two metasurfaces each performing first-order temporal differentiation can be cascaded to realize second-order differentiation (Fig. 6D, right bottom panel).

## 2.4 Spatio-temporal operations

As a natural extension of the scenarios considered in the previous section, we can also consider metamaterials performing simultaneous spatial and temporal operations on the input signal, which can be obtained when the transfer function  $t(k_x, k_y, \omega)$  in Eq. 9 has a nontrivial dependence with respect to both the spatial frequencies ( $k_x, k_y$ ) and the temporal frequency  $\omega$ . In particular, if we redefine the functional expression of the transfer function such that  $\tilde{t}(k_x, k_y, \omega - \omega_0) = t(k_x, k_y, \omega)$ , and we assume that  $\tilde{t}$  is a polynomial expression in  $k_x, k_y$  and  $\Omega \equiv \omega - \omega_0$ , we find that the linear operation imparted on the spatio-temporal envelope of the input signal  $E_{in}(x, y, t)$  is given by the operator

$$\mathcal{L} \equiv \tilde{t}(-i\partial_x, -i\partial_y, i\partial_t) \quad (18)$$

As practical examples, let us consider two cases that have been studied recently in the literature. For simplicity, we focus on the case in which the

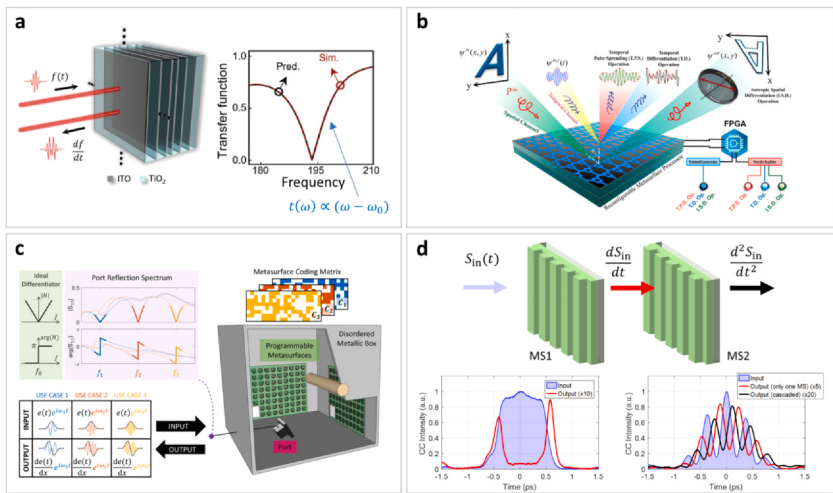


**Fig. 6 Metasurfaces that perform time-domain computational tasks.** (A) A Multi-layer metamaterial that calculates the first-order derivative. (B) Graphene-based multilayer metamaterial. (C) Radiofrequency metasurface performing first-order differentiation. (D) First experimental demonstration of an optical metasurface—made of titanium oxide—performing first-order differentiation at near-visible frequencies. (A) Adapted with permission from Knightley, T., Yakovlev, A., & Pacheco-Peña, V. (2022). Neural network design of multilayer metamaterial for temporal differentiation. *Advanced Optical Materials*, 11(5), 2202351. (B) Adapted with permission from Momeni, A., Rouhi, K., & Fleury, R. (2022). Switchable and simultaneous spatiotemporal analog computing with computational graphene-based multilayers. *Carbon*, 186, 599–611. (C) Adapted with permission from Sol, J., Smith, D. R., & Del Hougne, P. (2022). Meta-programmable analog differentiator. *Nature Communications*, 13(1), 1713. (D) Adapted with permission from Cotrufo, M., Esfahani, S., Korobkin, D., & Alù, A. (2024). Temporal Signal Processing with Nonlocal Optical Metasurfaces. *arXiv preprint arXiv: 2403.09087*.

transfer function does not depend on  $k_y$ , and thus it does not perform any operation involving spatial derivatives along the  $y$  direction.

We begin by considering the case, explored in refs. (Doskolovich, Kashapov, Bezas, & Bykov, 2022; Huang, Zhang, Zhu, & Ruan, 2022; Xu, Wang, Zhang, Dagens, & Zhang, 2021; Zhang, Ying, & Ruan, 2019; Zhou et al., 2021a; Zhou et al., 2023), in which the transfer function  $\tilde{t}(k_x, \omega - \omega_0) \propto C_x k_x + C_\omega (\omega - \omega_0)$  was studied, where  $C_x$  and  $C_\omega$  are complex coefficients. Following Eq. 18, a metasurface with such transfer function imparts the mathematical operation  $\mathcal{L} = -iC_x \partial_x + iC_\omega \partial_t$ , that is, a linear combination of first-order derivatives in space and time. Qualitatively, this response can be obtained if the metasurface features a transmission zero at normal incidence ( $k_x = 0$ ) and at a given frequency  $\omega = \omega_0$ , and such that the

transmission smoothly increases when either the frequency or the angle (or both) are varied (see, e.g., the left part of Fig. 7A). It has been shown (Doskolovich et al., 2022; Huang et al., 2022) that this type of response can be used to generate vortex beams carrying transversal orbital angular momentum (OAM), starting from input beams without spatial or temporal structure (i.e., quasi-planar waves). More broadly, this kind of spatio-temporal operations can be used to detect both spatial and temporal edges of the input image, that is, the spatio-temporal regions where the input intensity is strongly changing either in space or in time will be featured as high-intensity regions in the output image. However, given the fact that the spatial and temporal derivatives are summed, the operation cannot easily distinguish between spatial and temporal edges. In other words, high-intensity areas in the output image  $\mathcal{E}_{\text{out}}(x, y, t) \propto [-iC_x \partial_x + iC_\omega \partial_t]$   $\mathcal{E}_{\text{in}}(x, y, t)$  may be due either to fast variations of the input image in time, or to fast variations of the image in space, and there is not a way to tell them apart.

Another interesting functionality, explored by Esfahani and coauthors (Esfahani, Cotrufo, & Alù, 2024) (Fig. 7B), can be obtained if the metasurface transfer function is a product of the form  $\tilde{t}(k_x, \omega - \omega_0) \propto k_x^m (\omega - \omega_0)^n$ , leading to the mixed differential operator  $\mathcal{L} \propto (-i\partial_x)^m (i\partial_t)^n$ . To simplify the discussion, let us focus on the case  $m = n = 2$ , corresponding to the output field  $\mathcal{E}_{\text{out}}(x, y, t) = \partial_x^2 \partial_t^2 \mathcal{E}_{\text{in}}(x, y, t)$ . In this scenario, due to the mixed differential operation, the output field features a large intensity only if the input field  $\mathcal{E}_{\text{in}}(x, y, t)$  *simultaneously* varies in space *and* time. In other words, images that are stationary in time ( $\partial_t^2 \mathcal{E}_{\text{in}}(x, y, t) = 0$ ) do not lead to any output intensity, even if they feature strong spatial variations  $\partial_x^2 \mathcal{E}_{\text{in}}(x, y, t)$ . Similarly, input beams with no spatial structure ( $\partial_x^2 \mathcal{E}_{\text{in}}(x, y, t) = 0$ ) do not lead to any output signal, even in the presence of large temporal variations, that is, large values of  $\partial_t^2 \mathcal{E}_{\text{in}}(x, y, t)$ . This response can be leveraged to implement analog *event-based image processing*, since the metasurface imparts the desired spatial operation (in this case,  $\partial_x^2$ ) only at instants where the input image changes in time. As a possible application, a metasurface with such response can perform *event-based edge detection* (Esfahani et al., 2024) (Fig. 7B, right bottom panel): the edges of an object are enhanced only when the object is moving, which facilitates applications such as object tracking. These functionalities correspond to the conventional operations of *neuromorphic* or *event-based cameras*. These devices, rather than capturing information at regular intervals, respond to local changes of the input signal in time, which

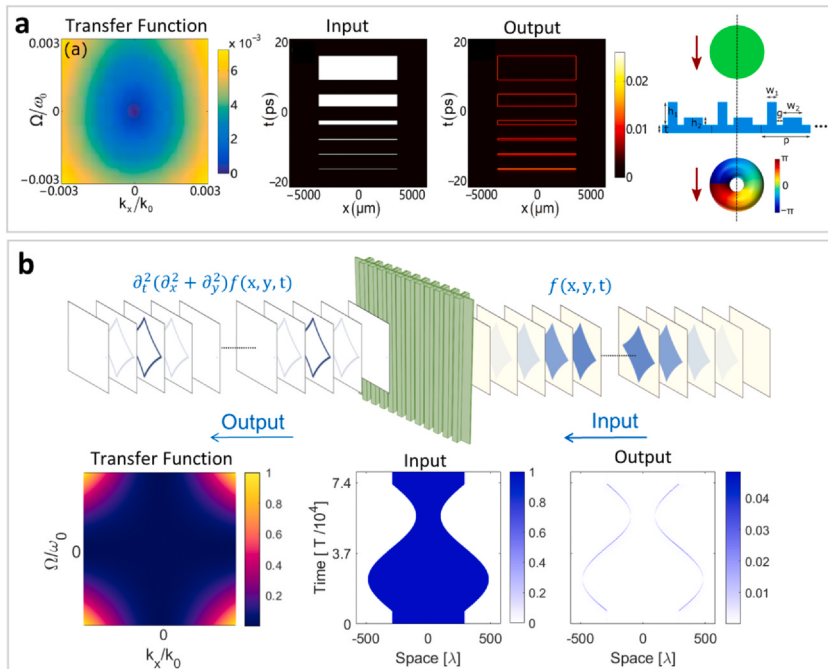


**Fig. 7** Metasurfaces that perform spatio-temporal computational tasks. (A) A metasurface with a transfer function proportional to  $C_x k_x + C_\omega (\omega - \omega_0)$  (left part) will perform the mathematical operation  $\mathcal{L} = -iC_x \partial_x + iC_\omega \partial_t$ . As a result, in the output image both spatial and temporal edges are enhanced (central part). The same metasurface can be used to generate vortex beams carrying transversal orbital angular momentum (right part). (B) A metasurface with a transfer function proportional to  $k_x^m (\omega - \omega_0)^n$  (bottom-left part) will apply the mixed derivative  $\mathcal{L} = \alpha (-i\partial_x)^m (i\partial_t)^n$  to the input image. As a result, in the output image (bottom-right part) only the spatio-temporal regions where the input image is simultaneously varying in space and time will be enhanced. (A) Adapted with permission from Huang, J., Zhang, J., Zhu, T., & Ruan, Z. (2022). Spatiotemporal differentiators generating optical vortices with transverse orbital angular momentum and detecting sharp change of pulse envelope. *Laser & Photonics Reviews*, 16(5), 2100357. (B) Adapted with permission from Esfahani, S., Cotrufo, M., & Alù, A. (2024). Space-Time nonlocal metasurfaces for event-based image processing. *arXiv preprint arXiv*, 2401.06586.

trigger data acquisition and processing. Current implementations of neuromorphic cameras require active components and voltage bias, preventing miniaturization and energy savings, while event-based metasurfaces operate in the analog domain with zero energy.

The transfer function  $\tilde{t}(k_x, \omega - \omega_0) \propto k_x^m (\omega - \omega_0)^n$  required to implement such mixed differential operators is typically more challenging

to implement than the sum of spatial and temporal operations. Similar to Fig. 7A, the metasurface must feature a transmission zero at normal incidence ( $k_x = 0$ ) and at a given frequency  $\omega = \omega_0$ . Now, however, the transmission amplitude must increase only when the angle of incidence *and* the frequency are simultaneously detuned, according to the product  $k_x^m (\omega - \omega_0)^n$ . In particular, the transmission should remain zero along the whole  $k_x = 0$  axis, that is, for any frequency, and along the whole  $\omega = \omega_0$  axis, that is, for any impinging angle, as shown in Fig. 7B (left). In ref (Esfahani et al., 2024), this response was obtained by cascading two metasurfaces which separately feature the responses  $\tilde{t}(k_x, \omega - \omega_0) \propto k_x^m$  and  $\tilde{t}(k_x, \omega - \omega_0) \propto (\omega - \omega_0)^n$ , and then by further optimizing the final geometry in order to minimize the impact of coupling between the two metasurfaces.

## 2.5 Pulse shapers and 4f optical systems with metasurfaces used as masks

The underlying advantage of the computational metasurfaces discussed in the previous sections is that they can manipulate the Fourier spectra of an input spatio-temporal signal without the need of Fourier-decomposing the input signal with the aid of additional bulk optics, leading to significant compactification compared to conventional analog-based image processing setups like those in Fig. 1. A sort of intermediate approach between these two scenarios has been explored in several works (Chen et al., 2022; Huo et al., 2020; Kim, Lee, Sung, Jang, & Lee, 2022; Tanriover, Dereshgi, & Aydin, 2023; Zhou et al., 2019; Zhou et al., 2021b). In these papers, a thin metasurface is used as a spatially varying mask inside either 4f systems (Huo et al., 2020; Kim et al., 2022; Tanriover et al., 2023; Zhou et al., 2019; Zhou et al., 2021b) or pulse shapers (Chen et al., 2022). These approaches are appealing because spatially varying metasurfaces allow tailoring the local transmission amplitude and phase more accurately than a conventional mask. This approach inherently leads to large operational spectral bandwidths in the context of spatial operations, since working in a 4f modality allows to effectively decouple spectral and angular responses much more easily than in a metasurface. Nonetheless, it is important to emphasize that these approaches are not fundamentally different from a standard 4f system and/or pulse shaper and, importantly, their intrinsic need for macroscopic optics strongly constrains their minimum footprint, alignment sensitivity, and limit the possibility of miniaturization. In other words, while the metasurface thickness can be sub-wavelength, in these approaches the

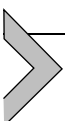
thickness of the mask/metasurface is far from being the limiting factor in determining the overall footprint of the processing system.



### 3. Tunable computational metasurafces

As discussed above, different metamaterial designs have been proposed and demonstrated to perform spatio-temporal image processing in compact systems, without the need of 4f optics and pulse shapers. However, most of the devices discussed here and demonstrated in the literature do not offer reconfigurability or programmability, which is a major limitation compared to conventional digital-based computing systems. In other words, the functionality of the devices discussed so far is fixed at the time of the implementation, and cannot be dynamically modified. Indeed, the possibility of reconfiguring the computational task is fundamental in order for these devices to replace digital computing in practical systems. To achieve this feature, it is necessary to introduce a controllable and reversible change of the optical properties of the material forming the metasurface. Reconfigurable and programmable responses have been demonstrated for metamaterials and metasurfaces operating at radio-frequencies (Sol et al., 2022; Zhang et al., 2020) and sub-THz frequencies (Lan et al., 2023). In these frequency ranges, the relatively large geometries and lattice pitches make it possible to control and reconfigure the response of each unit cell separately, by employing, for example, voltage-controlled capacitors and other circuit elements. This approach, however, is hard to scale down for metamaterials operating at optical frequencies, because of the much smaller spatial scales involved. Thus, other techniques need to be employed. Zhang et al. (2021) have demonstrated that mechanical strain can be leveraged to switch on and off the response of edge-detection metasurfaces (Fig. 8A). Several theoretical proposals (Khodasevych, Wesemann, Roberts, & Iacopi, 2023; Li et al., 2022b; Momeni et al., 2022; Xia, Yang, & Zhi, 2023) have suggested that large reconfigurability may be achieved by electrically gating a graphene layer placed above or inside a metasurface (Fig. 8B). Similar approaches have been experimentally demonstrated by employing liquid crystals (Xiao et al., 2022; Yin et al., 2021), although so far only for metasurfaces used as masks in 4f systems. Reconfigurability can also be achieved by leveraging material nonlinearities. For example, Zhou et al (Zhou et al., 2022) demonstrated a metasurface made of a saturable material (Fig. 8C)—a stack of multi-

quantum wells—that performs edge detection for low input powers, while for large input powers the output image remains unprocessed. Theoretical studies have also proposed controlling the metasurface operation via an external optical pump (Iushkov, Shorokhov, & Fedyanin, 2021). The metasurface response can also be controlled by temperature (Rahmani et al., 2017), for example by leveraging the fact that, due to thermo-optic effects, the refractive index of most materials varies with temperature. While this method is appealing because of its universality and ease of implementation, it also suffers from the fact that, typically, temperature variations of several tens or hundreds of degrees are necessary in order to obtain sizeable effects (Rahmani et al., 2017). Several studies (Abdollahramezani et al., 2022; Heenkenda, Hirakawa, & Sarangan, 2021; King et al., 2024; Park, Kim, Landreman, & Brongersma, 2020; Tripathi et al., 2022) have been showing that the response of a metasurface can be made strongly dependent on small temperature variations by using phase-change materials. These materials, such as vanadium dioxide ( $\text{VO}_2$ ) (Taha et al., 2017), antimony trisulfide ( $\text{Sb}_2\text{S}_3$ ) and germanium antimony telluride, experience abrupt changes of their crystalline structure as the temperature exceeds a certain threshold. This sudden change of crystal structure results in a strong variation of the optical properties, thus making such materials appealing for reconfigurable photonics. In the field of computational metasurfaces, Cotrufo et al. (2023) have recently demonstrated that, by embedding a thin layer of  $\text{VO}_2$  within a silicon metasurface, an edge-detection metasurface can be realized with image processing functionality being turned on and off by temperature variations smaller than 10 °C around a CMOS-compatible temperature of 65 °C (Fig. 8D). This was realized by a design metasurface whose angle-dependent transfer function (Fig. 8D, left) is strongly reconfigured when the  $\text{VO}_2$  transitions from the insulating to the metallic phase.



#### 4. Nonlinear computational metamaterials

All devices discussed in the previous sections are linear, since the output field is related to the input field via a linear operator. This is inherently connected to the fact that the optical response of most materials is linear for low input intensities. A natural extension of this framework is to investigate whether nonlinear optical materials can be used to implement nonlinear mathematical operations. As a first step towards this opportunity, de Ceglia and coauthors (de Ceglia, Alù, Neshev, & De Angelis, 2024) have recently pointed out that a thin layer of unpatterned nonlinear material can

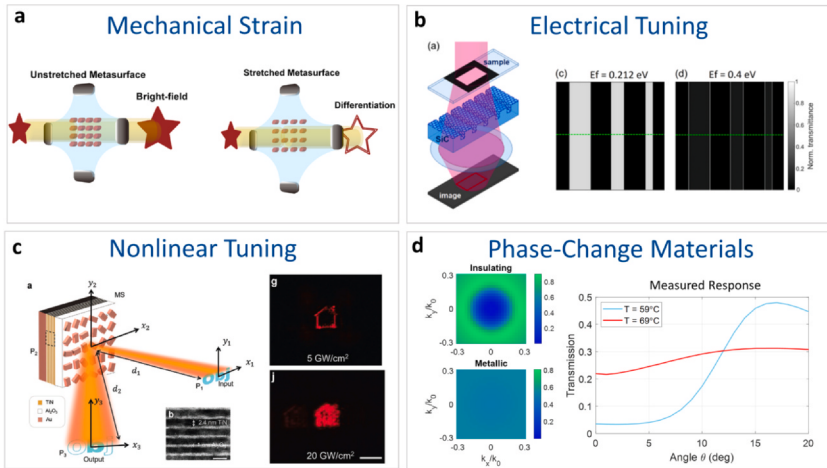


**Fig. 8** Reconfigurable computational metasurfaces. (A) By applying mechanical strain to a metasurface, the computational task can be switched between bright-field imaging and differentiation. (B) Several theoretical works have proposed using flat materials such as SiC and graphene to perform electrical tuning. (C) If the metasurface is made of a material with a saturable-absorption response (e.g., multi-quantum wells), the image processing imparted on the input image depends on the input intensity. (D) By using phase-change materials, it is possible to realize computational metasurfaces whose response can be strongly reconfigured with temperature changes smaller than 10 degrees Celsius. (A) Adapted with permission from Zhang, X., Zhou, Y., Zheng, H., Linares, A. E., Ugwu, F. C., Li, D., Sun, H.B., Bai, B., & Valentine, J. G. (2021). Reconfigurable metasurface for image processing. *Nano Letters*, 21(20), 8715–8722. (B) Adapted with permission from Khodasevych, I., Wesemann, L., Roberts, A., & Iacopi, F. (2023). Tunable nonlocal metasurfaces based on graphene for analogue optical computation. *Optical Materials Express*, 13(5), 1475–1487. (C) Adapted with permission from Zhou, J., Zhao, J., Wu, Q., Chen, C. F., Lei, M., Chen, G., ... & Liu, Z. (2022). Nonlinear computational edge detection metasurface. *Advanced Functional Materials*, 32(34), 2204734. (D) Adapted with permission from Cotrufo, M., Sulejman, S. B., Wesemann, L., Rahman, M. A., Bhaskaran, M., Roberts, A., & Alù, A. (2023). Reconfigurable image processing metasurfaces with phase-change materials. *arXiv preprint arXiv:2311.13109*.

be used to perform nonlinear Fourier filtering. In particular, it was theoretically shown (de Ceglia et al., 2024) that, if an image  $\mathbf{E}_{\text{in}}(x, y, t) = \mathbf{E}_{\text{in}}(x, y, t) e^{i\omega_0 t} \mathbf{e}_{\text{in}}$  impinges on a thin slab of nonlinear material with a configuration similar to the one sketched in Fig. 2, and the nonlinear  $\chi^{(2)}$  tensor of the material is such that only the  $zzz$  component is nonzero, then the nonlinear second-harmonic polarization density

$$P_z^{(2\omega_0)}(x, y) = \epsilon_0 \chi_{zzzz}^{(2)} \quad \mathcal{F}^{-1}[E_z(\mathbf{k}_\parallel)^* E_z(\mathbf{k}_\parallel)] \quad (19)$$

is generated, where  $E_z(\mathbf{k}_{\parallel})$  denotes the z-component of the plane-waves generated by the image and propagating at a direction identified by  $\mathbf{k}_{\parallel}$ . The symbol  $*$  denotes the convolution product. The polarization density  $P_z^{(2\omega_0)}$  generates a second-harmonic image at frequency  $2\omega_0$ , denoted with  $\mathbf{E}_{\text{out}}^{(2\omega_0)}(x, y)$ , which propagates along the same direction as the original image (Fig. 9A). Equation 19 shows that the spatial shape of  $P_z^{(2\omega_0)}(x, y)$  is determined nonlinearly by the spatial Fourier components of the input image. For example, when the input field (at  $\omega_0$ ) is  $x$ -polarized, it can be shown that the components of the output image  $\mathbf{E}_{\text{out}}^{(2\omega_0)}(x, y)$  are (de Ceglia et al., 2024)

$$E_x^{(2\omega_0)}(x, y) \propto 2 \frac{\partial \mathcal{E}_{\text{in}}(x, y)}{\partial x} \frac{\partial^2 \mathcal{E}_{\text{in}}(x, y)}{\partial x^2} \quad (20)$$

$$E_y^{(2\omega_0)}(x, y) \propto \frac{\partial}{\partial y} \left[ \frac{\partial \mathcal{E}_{\text{in}}(x, y)}{\partial x} \right]^2 \quad (21)$$

The output image depends on the gradients of the input image, and it can be used for edge detection. Now however the dependence between the output fields and the gradients of the input field is nonlinear, which unlocks the possibility of implementing more general nonlinear mathematical operations. For the specific application of edge detection, this nonlinear approach has appealing advantages, such as ease of fabrication (because no patterning is required) and, most importantly, very broad spectral bandwidths: since no resonant phenomena are required to support Eq. 19, the device is now agnostic to the excitation frequency. The only practical limitation on the spectral bandwidth of this processing operation comes from absorption at either the fundamental frequency or at the second harmonic within the nonlinear material. Also the NA of these device is also not fundamentally limited. On the other hand, the absence of any resonant effect, combined with the typically low generation efficiency of thin films, results in a low throughput efficiency: the intensity of the output image is typically several orders of magnitude smaller than the intensity of the input image. The theoretical prediction in (de Ceglia et al., 2024). has been demonstrated experimentally (Cotrufo) with a thin slab of gallium arsenide (Fig. 9B), showing nonlinear edge detection for any pump wavelength between 1400 and 1700 nm, only limited by the absorption of the corresponding second-harmonic signal.

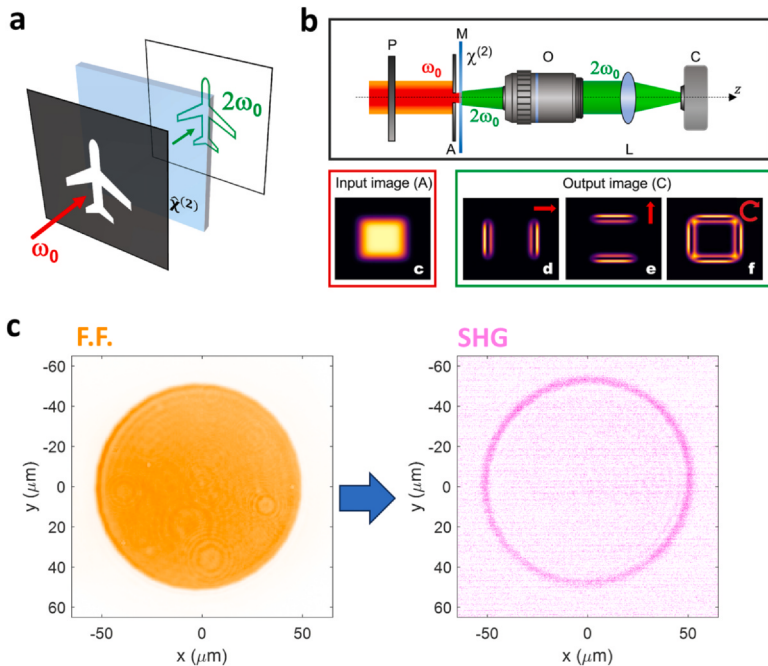
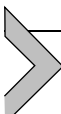


**Fig. 9** Nonlinear all-optical computation. (A–B) An image at frequency  $\omega_0$  impinges on a thin sheet of nonlinear material, generating a second-harmonic image at frequency  $2\omega_0$ . The features of the output image are determined by the symmetries and non-zero-elements of the nonlinear  $\chi^{(2)}$  tensor. (C) Experimental demonstration of these effects with a thin slab of Gallium Arsenide. (A–B) Adapted with permission from de Ceglia, D., Alù, A., Neshev, D. N., & De Angelis, C. (2024). Analog image processing with nonlinear nonlocal flat optics. *Optical Materials Express*, 14(1), 92–100. (C) Adapted with permission from Cotrufo, M. et al. (2024). In preparation.



## 5. Final remarks and outlook

Metasurfaces have been offering unprecedented opportunities to manipulate the optical wavefront, and more recently they have been shown to be capable to perform spatio-temporal image and optical processing within passive, compact and ultrafast devices. This capability is intimately connected to the possibility of shaping the angle- and frequency-dependent transfer function of a metasurface, which allows performing Fourier filtering without having to physically decompose the signal in the Fourier space and then map its Fourier decomposition on another plane.

In this chapter, we have discussed the basic working principles of metasurfaces performing spatial, temporal, and spatio-temporal operations, and we

have reviewed recent breakthroughs in the field. Moreover, we have discussed recent proposals to realize reconfigurable computational metasurfaces, and to extends these concepts to the realm of nonlinear optics.

Despite the exciting results demonstrated so far in the field of computational metasurfaces, there are still several challenges that need to be addressed for this platform to become relevant for practical applications. The most common approach to tailor the metasurface transfer function—that is, inducing and controlling sharp resonances—introduces several trade-offs between different figures of merit. For example, it is challenging to achieve large spectral bandwidths while simultaneously maintaining high intensity throughputs. Similarly, large numerical apertures (which are necessary to be able to process high-resolution images) are often accompanied by large anisotropies and polarization asymmetries. Promising approaches to optimize all these figures of merit simultaneously have been proposed based on dispersion engineering ([Cotrufo, Arora et al., 2023](#)), yet a general route to optimize all these metrics fully and independently is still lacking.

The intensity throughput of these devices—that is, how the intensity of the processed image compares to the intensity of the input image—is of fundamental importance. Yet, this metric is often overlooked in experimental works, which only report the input and output intensities in arbitrary units. A proper quantitative assessment of this metric will be critical towards their implementation in real-world application, and we have discussed possible ways of measuring it. Another important challenge to overcome is the capability of dynamically reconfiguring and programming the response of a metasurface. For metasurfaces at radio-frequencies and sub-THz frequencies, it is relatively easy to dynamically control the response of each unit cell, and very refined programmable metasurfaces have been demonstrated. At optical frequencies, these approaches are more challenging due to the reduced spatial scales. In this frequency range, several approaches have been proposed to obtain reconfigurable computational metasurfaces, based on changing the optical properties of materials via, for example, mechanical, thermal, electro-optics and nonlinear effects. However, most of the devices demonstrated so far allow only a binary switching between two computational tasks, for example, switching between performing edge detection of an image and not performing any operation. Full programmability, that is, being able to reconfigure the response of a metasurface within a continuous a nontrivial set of tasks, is still out of reach for devices operating at optical frequencies.

## Acknowledgements

This work was supported by the Air Force Office of Scientific Research MURI program and the Simons Foundation.

## References

- Abdollahramezani, S., et al. (2022). Electrically driven reprogrammable phase-change metasurface reaching 80% efficiency. *Nature Communications*, *13*, 1696.
- Bykov, D. A., Doskolovich, L. L., Bezus, E. A., & Soifer, V. A. (2014). Optical computation of the Laplace operator using phase-shifted Bragg grating. *Optics Express*, *22*, 25084.
- de Ceglia, D., Alù, A., Neshev, D. N., & De Angelis, C. (2024). Analog image processing with nonlinear nonlocal flat optics. *Optical Materials Express*, *14*, 92–100.
- Chen, L., et al. (2022). Synthesizing ultrafast optical pulses with arbitrary spatiotemporal control. *Science Advances*, *8*, eabq8314.
- Collin, R. E. (1985). *Antennas and radiowave propagation*. McGraw-Hill.
- Cordaro, A., et al. (2019). High-Index dielectric metasurfaces performing mathematical operations. *Nano Letters*, *19*, 8418–8423.
- Cotrufo, M., Arora, A., Singh, S., & Alù, A. (2023). Dispersion engineered metasurfaces for broadband, high-NA, high-efficiency, dual-polarization analog image processing. *Nature Communications*, *14*, 7078.
- Cotrufo, M., Singh, S., Arora, A., Majewski, A., & Alù, A. (2023). Polarization imaging and edge detection with image-processing metasurfaces. *Optica*, *10*, 1331–1338.
- Cotrufo, M., Esfahani, S., Korobkin, D., & Alù, A. (2024). Temporal signal processing with nonlocal optical metasurfaces. *arXiv preprint arXiv:2403.09087*.
- Cotrufo, M., et al. (2023). Reconfigurable image processing metasurfaces with phase-change materials. *arXiv preprint arXiv:2311.13109*.
- Cotrufo, M. et al. (n.d.) In preparation.
- Doskolovich, L. L., Kashapov, A. I., Bezus, E. A., & Bykov, D. A. (2022). Spatiotemporal optical differentiation and vortex generation with metal-dielectric-metal multilayers. *Physical Review A*, *106*, 033523.
- Esfahani, S., Cotrufo, M., & Alù, A. (2024). Space-Time nonlocal metasurfaces for event-based image processing. *arXiv preprint arXiv:2401.06586*.
- Goodman, J. W. (1996). *Introduction to fourier optics*. New York: McGraw-Hill.
- Guo, C., Xiao, M., Minkov, M., Shi, Y., & Fan, S. (2018). Photonic crystal slab Laplace operator for image differentiation. *Optica*, *5*, 251.
- He, C., et al. (2021). Polarisation optics for biomedical and clinical applications: A review. *Light: Science & Applications*, *10*, 194.
- Heenkenda, R., Hirakawa, K., & Sarangan, A. (2021). Tunable optical filter using phase change materials for smart IR night vision applications. *Optics Express*, *29*, 33795–33803.
- Huang, J., Zhang, J., Zhu, T., & Ruan, Z. (2022). Spatiotemporal differentiators generating optical vortices with transverse orbital angular momentum and detecting sharp change of pulse envelope. *Laser & Photonics Reviews*, *16*, 2100357.
- Huo, P., et al. (2020). Photonic spin-multiplexing metasurface for switchable spiral phase contrast imaging. *Nano Letters*, *20*, 2791–2798.
- Iushkov, V., Shorokhov, A., & Fedyanin, A. (2021). *Tunable GaAs metasurfaces for ultrafast image processing*. *Journal of Physics: Conference Series*, IOP Publishing, 2015, 012057.
- Ji, A., et al. (2022). Quantitative phase contrast imaging with a nonlocal angle-selective metasurface. *Nature Communications*, *13*, 7848.
- Khodasevych, I., Wesemann, L., Roberts, A., & Iacopi, F. (2023). Tunable nonlocal metasurfaces based on graphene for analogue optical computation. *Optical Materials Express*, *13*, 1475–1487.

- Kim, Y., Lee, G.-Y., Sung, J., Jang, J., & Lee, B. (2022). Spiral metalens for phase contrast imaging. *Advanced Functional Materials*, *32*, 2106050.
- King, J., et al. (2024). Electrically tunable VO<sub>2</sub>-metal metasurface for mid-infrared switching, limiting and nonlinear isolation. *Nature Photonics*, *18*, 74–80.
- Knightley, T., Yakovlev, A., & Pacheco-Peña, V. (2022). Neural network design of multilayer metamaterial for temporal differentiation. *Advanced Optical Materials*, *11*.
- Komar, A., et al. (2021). Edge detection with Mie-resonant dielectric metasurfaces. *ACS Photonics*, *8*, 864–871.
- Kwon, H., Cordaro, A., Sounas, D., Polman, A., & Alù, A. (2020). Dual-Polarization analog 2D image processing with nonlocal metasurfaces. *ACS Photonics*, *7*, 1799–1805.
- Kwon, H., Sounas, D., Cordaro, A., Polman, A., & Alù, A. (2018). Nonlocal metasurfaces for optical signal processing. *Physical Review Letters*, *121*, 173004.
- Lan, F., et al. (2023). Real-time programmable metasurface for terahertz multifunctional wave front engineering. *Light: Science & Applications*, *12*, 191.
- Li, H., et al. (2022a). Performing calculus with epsilon-near-zero metamaterials. *Science Advances*, *8*, eabq6198.
- Li, Q., et al. (2022b). Gate-tuned graphene meta-devices for dynamically controlling terahertz wavefronts. *Nanophotonics*, *11*, 2085–2096.
- Momeni, A., Rouhi, K., & Fleury, R. (2022). Switchable and simultaneous spatiotemporal analog computing with computational graphene-based multilayers. *Carbon*, *186*, 599–611.
- Park, J., Kim, S. J., Landreman, P., & Brongersma, M. L. (2020). An over-coupled phase-change metasurface for efficient reflection phase modulation. *Advanced Optical Materials*, *8*, 2000745.
- Rahmani, M., et al. (2017). Reversible thermal tuning of all-dielectric metasurfaces. *Advanced Functional Materials*, *27*, 1700580.
- Rubin, N. A., et al. (2022). Imaging polarimetry through metasurface polarization gratings. *Optics Express*, *30*, 9389–9412.
- Silva, A., et al. (2014). Performing mathematical operations with metamaterials. *Science (New York, N. Y.)*, *343*, 160–163.
- Solomon, J. E. (1981). Polarization imaging. *Applied Optics*, *20*, 1537–1544.
- Sol, J., Smith, D. R., & del Hougne, P. (2022). Meta-programmable analog differentiator. *Nature Communications*, *13*.
- Taha, M., et al. (2017). Insulator–metal transition in substrate-independent VO<sub>2</sub> thin film for phase-change devices. *Scientific Reports*, *7*, 17899.
- Tahmasebi, O., Abdolali, A., Rajabalipanah, H., Momeni, A., & Fleury, R. (2022). Parallel temporal signal processing enabled by polarization-multiplexed programmable THz metasurfaces. *Optics Express*, *30*, 45221–45232.
- Tanriover, I., Dereshgi, S. A., & Aydin, K. (2023). Metasurface enabled broadband all optical edge detection in visible frequencies. *Nature Communications*, *14*, 6484.
- Tripathi, A., et al. (2022). *Nanoscale optical nonreciprocity with nonlinear metasurfaces*. <https://arxiv.org/abs/2210.14952>.
- Tyo, J., Rowe, M., Pugh, E., & Engheta, N. (1996). Target detection in optically scattering media by polarization-difference imaging. *Applied Optics*, *35*, 1855–1870.
- Wang, H., Guo, C., Zhao, Z., & Fan, S. (2020). Compact incoherent image differentiation with nanophotonic structures. *Ac Photonics*, *7*, 338–343.
- Weiner, A. M. (2011). Ultrafast optical pulse shaping: A tutorial review. *Optics Communications*, *284*, 3669–3692.
- Weiner, A. M. (2000). Femtosecond pulse shaping using spatial light modulators. *Review of Scientific Instruments*, *71*, 1929–1960.
- Weiner, A. M., Heritage, J. P., & Kirschner, E. (1988). High-resolution femtosecond pulse shaping. *JOSA B*, *5*, 1563–1572.

- Wesemann, L., et al. (2019). Selective near-perfect absorbing mirror as a spatial frequency filter for optical image processing. *APL Photonics*, *4*, 100801.
- Wesemann, L., et al. (2021). Nanophotonics enhanced coverslip for phase imaging in biology. *Light: Science & Applications*, *10*, 98.
- Xiao, T., et al. (2022). Realization of tunable edge-enhanced images based on computing metasurfaces. *Optics Letters*, *47*, 925–928.
- Xia, D., Yang, J., & Zhi, Q. (2023). Electrically tunable optical spatial differentiation with graphene. *Optics Express*, *31*, 27312–27323.
- Xue, W., & Miller, O. D. (2021). High-NA optical edge detection via optimized multilayer films. *Journal of Optics*, *23*, 125004.
- Xu, C., Wang, Y., Zhang, C., Dagens, B., & Zhang, X. (2021). Optical spatiotemporal differentiator using a bilayer plasmonic grating. *Optics Letters*, *46*, 4418–4421.
- Yin, Y., et al. (2021). High-dynamic-resolution optical edge detection based on liquid crystal diffractive moiré lenses with a tunable focal length. *Optics Letters*, *46*, 2549–2552.
- Zhang, X., Bai, B., Sun, H.-B., Jin, G., & Valentine, J. (2022). Incoherent optoelectronic differentiation based on optimized multilayer films. *Laser & Photonics Reviews*, *16*, 2200038.
- Zhang, J., Ying, Q., & Ruan, Z. (2019). Time response of plasmonic spatial differentiators. *Optics Letters*, *44*, 4511.
- Zhang, X. G., et al. (2020). An optically driven digital metasurface for programming electromagnetic functions. *Nature Electronics*, *3*, 165–171.
- Zhang, X., et al. (2021). Reconfigurable metasurface for image processing. *Nano Letters*, *21*, 8715–8722.
- Zhou, Y., Zheng, H., Kravchenko, I. I., & Valentine, J. (2020). Flat optics for image differentiation. *Nature Photonics*, *14*, 316–323.
- Zhou, Y., et al. (2021a). Analogue optical spatiotemporal differentiator. *Advanced Optical Materials*, *9*, 2002088.
- Zhou, J., et al. (2021b). Two-dimensional optical spatial differentiation and high-contrast imaging. *National Science Review*, *8*, nwaa176.
- Zhou, Y., et al. (2023). Electromagnetic spatiotemporal differentiation meta-devices. *Laser & Photonics Reviews*, *17*, 2300182.
- Zhou, J., et al. (2019). Optical edge detection based on high-efficiency dielectric metasurface. *Proceedings of the National Academy of Sciences of the United States of America*, *116*, 11137–11140.
- Zhou, J., et al. (2022). Nonlinear computational edge detection metalens. *Advanced Functional Materials*, *32*, 2204734.
- Zhu, T., et al. (2019). Generalized spatial differentiation from the spin hall effect of light and its application in image processing of edge detection. *Physical Review Applied*, *11*, 034043.
- Zhu, T., et al. (2017). Plasmonic computing of spatial differentiation. *Nature Communications*, *8*, 15391.
- Zhu, T., et al. (2021). Topological optical differentiator. *Nature Communications*, *12*, 680.